Five-Dimensional Incommensurate Structure of the Melilite Electrolyte [CaNd]2[Ga]2[Ga2O7]2

Wei, Fengxia; Baikie, Tom; An, Tao; Schreyer, Martin; Kloc, Christian; White, Timothy John

2011

https://hdl.handle.net/10356/85606

https://doi.org/10.1021/ja206441x

Downloaded on 04 Apr 2024 06:07:58 SGT

The Five-Dimensional Incommensurate Structure of the Melilite Electrolyte [CaNd]$_2$[Ga]$_2$[Ga$_2$O$_7$]$_2$

Fengxia Wei[a], Tom Baikie[a*], Tao An[a], Martin Schreyer[b], Christian Kloc[a] and Tim. J. White[a,c]

[a] Division of Materials Science & Engineering, Nanyang Technological University, Singapore.

[b] Institute of Chemical Engineering Sciences (ICES), Agency for Science, Technology and Research, 1 Pesek Road, Jurong Island, 627833, Singapore

[c] Centre for Advanced Microscopy, Australian National University, Sullivan's Creek Road, Canberra, ACT 0200 Australia

* Corresponding author –tbaikie@ntu.edu.sg

Abstract

Melilite-type gallium oxides are potential intermediate temperature electrolytes for solid oxide fuel cells. Single crystals of [CaNd]$_2$[Ga]$_2$[Ga$_2$O$_7$]$_2$ grown using an optical floating zone furnace have been investigated using transmission electron microscopy, powder and single crystal X-ray diffraction. The anion array topologically conforms to a [(3.5.4.5)^2, 3.5.3.5] network that contains distorted pentagonal tunnels. The distortion is necessary to achieve space filling and accommodate structural misfit between the layers. Satisfactory

bond lengths and angles are obtained through two-dimensional modulation in the tetragonal based plane, leading to five-dimensional symmetry in the superspace group $P\bar{4}2_1m(\alpha,\alpha,0)00s(\bar{\alpha},\alpha,0)000$, $\alpha = 0.2319(2)$ and modulation vectors: $\boldsymbol{q}_1 = \alpha\,(\boldsymbol{a}^* + \boldsymbol{b}^*)$, $\boldsymbol{q}_2 = \alpha\,(-\boldsymbol{a}^* + \boldsymbol{b}^*)$. Both displacive and occupational modulations are found. Through this mechanism, melilites are primed to accommodate mobile oxygen interstitials, suggesting a rational approach to crystallochemical tailoring that will enhance ionic diffusion and optimize electrolyte performance.

Introduction

Solid oxide fuel cells (SOFC) are an efficient and low polluting energy conversion technology. A focus of current research is to reduce SOFC operating temperatures to ~ 500°C through deployment of highly conductive electrolytes. Usually, oxygen transport is mediated via anionic vacancies, typically, in yttria stabilized zirconia (YSZ) and gadolinium doped ceria.[1] However, in some materials oxide ions conduct via an interstitial mechanism at 'intermediate' temperatures.[2] Of particular interest are the apatite,[3] fergusonite[4] and melilite families,[5, 6] which contain mobile superstoichiometric oxygen. Those structures often show non-rational crystallographic translations, not accommodated within standard three dimensional crystallographic space groups, but rather superspace groups, which describe periodicity in 4-, 5-, and 6-dimensions.[7] Numerous materials are now classified as higher dimensional structures including Na_2CO_3,[8] intermetallic quasicrystals[9] and cuprate high temperature superconductors,[10] along with certain apatites,[11] fergusonites,[12] and melilites.[13] Of the latter structure types, the melilite family is currently the most broadly understood in terms of

2

incommensurability and ion conduction, but a direct causal link between crystal chemistry and electrolyte performance remains to be established.

To a first approximation, melilites adopt tetragonal $P\bar{4}2_1m$ symmetry, and have the general formula $[A_2]_2[B^I]_2[B^{II}_2O_7]_2$ where A are large divalent or trivalent ions (e.g. Ln, Ca, Sr and Ba) and B^I, B^{II} are symmetrically distinct small cations (e.g. Si and Ge). Two dimensional extended oxygen networks of the type $[(3.5.4.5)^2, 3.5.3.5]$ are created by corner-connection of B^IO_4 and $B^{II}_2O_7$ units, with these layers separated by AO_8 polyhedra.[14] This structural framework can accommodate a large excess of oxygen, up to 0.32 per formula unit (e.g. $[Ca_{0.36}La_{1.64}]_2[Ga]_2[Ga_2O_{7.32}]_2$),[15] believed responsible for the high ion conductivity. Misfit of the tetrahedral layers with the interlayer cations is accommodated by atomic displacements, leading to incommensuration, that has been extensively studied in natural and synthetic silicate-melilites,[13] but not so deeply for electrolyte compositions. Seifert et $al.$[16] analyzed åkermanite ($[Ca_2]_2[Mg]_2[Si_2O_7]_2$) using ^{29}Si magic angle spinning nuclear magnetic resonance (MAS NMR) spectroscopy and found an incommensurate to commensurate phase transition at 78°C. Synthetic $[Ca_2]_2[Co]_2[Si_2O_7]_2$ (Co-åkermanite) was found to be modulated using single crystal X-ray diffraction,[17] and soon after, the solid solutions of $[(Sr/Ca)]_2[Co/Zn/Mg]_2[Si_2O_7]_2$ were described[18-21], with specific combinations of A and/or B^I site substitutions resulting in modulation. Bindi et $al.$[22] reported a natural melilite ($[Ca_{1.89}Sr_{0.01}Na_{0.08}K_{0.02}]_2[Mg_{0.92}Al_{0.08}]_2[Si_{1.97}Al_{0.03}O_7]_2$) was also modulated, while transmission electron microscopy (TEM) defined the incommensurate to commensurate phase transition temperatures of $[(Sr/Ca)]_2[(Co/Mg/Zn/Fe/Cu)]_2[(Si/Ge)_2O_7]_2$

compositions.[13] Almost all previous work has focused on substitutions at the *A* (*4e*) and B^I (*2a*) cation sites.

As recently shown, the gallate melilite $[Sr_{0.46}La_{1.54}]_2[Ga]_2[Ga_2O_{7.27}]_2$ possesses high oxide conductivity (0.02-0.1Scm^{-1}) over the temperature range 600-900°C,[5, 15, 23, 24] and for the $[Ca_{1-x}La_{1+x}]_2[Ga]_2[Ga_2O_{7+x/2}]_2$ series phase transitions from tetragonal ($x \leq 0.5$) to orthorhombic ($0.5 < x \leq 0.6$) to triclinic symmetry ($0.6 < x \leq 0.64$) were found as lanthanum content increased.[15] It was also observed that $x > 0.5$ gave lower conductivities, attributed to the reduction of symmetry, however, no information concerning the nature of the incommensurate modulation in these gallium melilites was provided. Here, we report for the first time the 5D incommensurate structure of the gallium oxide melilite $[CaNd]_2[Ga]_2[Ga_2O_7]_2$ using superspace formalism,[25] and consider the implications with respect to preferential oxygen ion migration pathways, tailoring interstitial oxygen content and enhancing ion mobility.

Experimental Details

Powder Synthesis

Single crystals of $[CaNd]_2[Ga]_2[Ga_2O_7]_2$ were grown using an optical floating zone furnace. In 10 gram batches, stoichiometric mixtures of Nd_2O_3 (99.99% Alfa Aesar), $CaCO_3$ (99.9%, Alfa Aesar) and Ga_2O_3 (99.999%, Aldrich) were ground and homogeneously mixed in ethanol, dried in air (100°C/6 hours), then fired (800°C/10 hours) to decompose $CaCO_3$. The Nd_2O_3 was dehydrated and decarbonated (1000°C/6 hours) before use. The calcines were reground, pressed into pellets and sintered (1400 °C/12 hours) to yield single phase products according to powder X-ray diffraction

(see below). For these experiments, a neodymium melilite rather than the lanthanum analogue was prepared, as the blue color of the former better absorbs infrared radiation which simplifies single crystal growth.

Single crystal growth

The polycrystalline materials were isostatically pressed into duplicate cylinders (5cm ×0.5cm), to serve as the feed and seed rods, and sintered (1400°C/6 hours) before mounting in the mirror furnace. Crystal growth took place in an FZ-T-4000-H-VPO-VII-PC optical floating zone furnace (Crystal Systems Corporation, Japan) containing four 1.5 kW halogen lamps, with corresponding ellipsoidal mirrors to focus the infrared irradiation to a region ~5 mm in extent, while a constant flow of dry air (2 L/min) passed through the growth chamber. With the onset of melting, tips of the feed and seed rods were brought into contact to form the floating-zone, and upon stabilization, the entire mirror stage was raised at a rate of 5 mm/h for crystal growth. The rods were counter-rotated at constant speed (27 rpm) to maintain a stable and well-mixed molten zone. Initially, polycrystalline rods were used as seeds, however, once an appreciable single crystal was obtained, it was cut and oriented with c parallel to the growth direction for subsequent experiments.

Structural Characterization

Powder X-Ray Diffraction: The top and bottom parts of the single crystal rods were cut and ground for analysis by powder X-ray diffraction (PXRD) to confirm melilite synthesis and check for secondary phases. The PXRD patterns were collected on a Bruker Advance D8 X-ray diffractometer (Cu $K\alpha$, $\lambda_{av} = 1.54187$Å) equipped with a Cu $K\alpha$ X-ray tube operated at 40 kV and 40 mA. The crushed powders were mounted in a

top-loaded trough and data accumulated from 5-140° 2θ using a step size of 0.02° with a dwell time of 1s per step. Under these conditions the intensity of the strongest peak was ≈ 30000 counts (Figure 1). Rietveld refinement of the patterns was carried out with *TOPAS V4.1,*[26] using the fundamental parameters approach[27] and a full axial divergence model.[28] The data were refined from the average three dimensional structure ($P\bar{4}2_1m$), based on the atomic positions of Skakle *et al.*[29], in addition to the zero error, Chebyshev polynomial fitting of the background, and the 'Crystallite Size' to account for microstructure-controlled line broadening. Only isotropic atomic displacement parameters (ADPs) were refined with a common ADP taken for all O positions and Nd and Ca occupying the same crystallographic site.
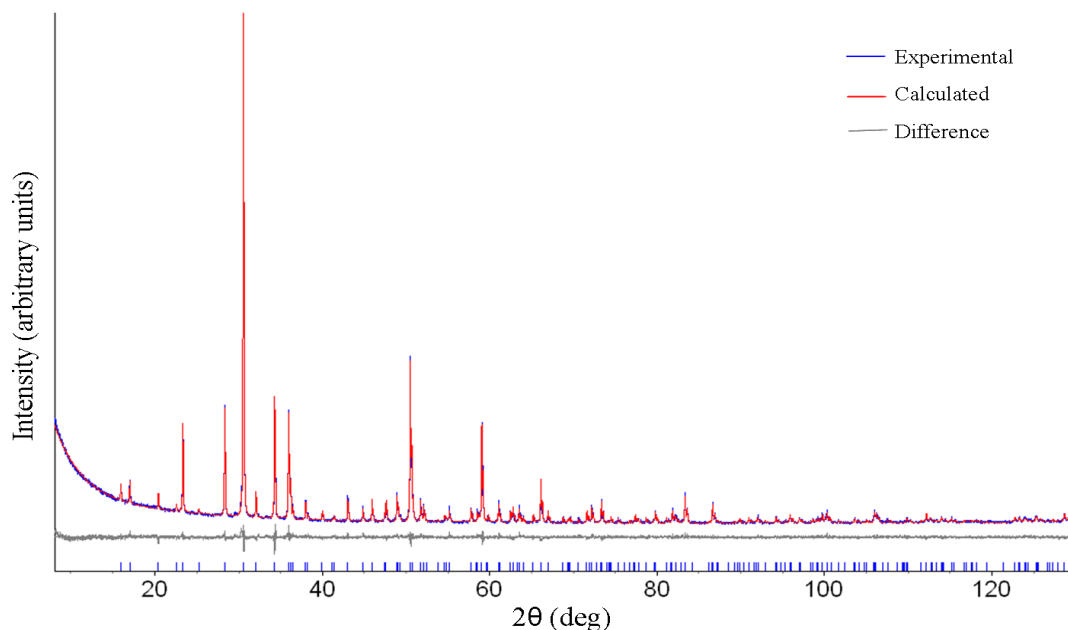

Figure 1. PXRD Rietveld refinement for the $[CaNd]_2[Ga]_2[Ga_2O_7]_2$ subcell (R_B =1.6%).

Single Crystal X-ray Diffraction: A single crystal fragment (0.1mm×0.08mm×0.15mm) was cleaved and mounted on a glass fiber. Data was collected on a Bruker Smart Apex II single crystal diffractometer (X-ray radiation Mo *Kα*,

λ=0.71073Å), over an angular range of 2.07°≤θ≤33.68°, with an exposure time of 200s/degree to give a total collection time of ~50 hours. The modulation vectors were calculated by the least-squares method from 1891 satellites, and reflections indexed with Apex II software using five integer values. The Saint module, deployed within Apex II, was used for reflection integration, performing Lorentz polarization and multi-scan absorption corrections. The data were refined using Jana 2006[30] and no extra absorption correction was applied.

Selected Area Electron Diffraction: Selected area electron diffraction patterns (SAED) of single crystals were obtained from powders finely crushed under ethanol with several drops of the suspension deposited on a holy carbon mesh supported by a copper grid. A JEOL field emission TEM 2100F operated at 200 kV and fitted with a CCD camera was used to record the diffraction patterns. A Gatan double tilt holder was employed to tilt crystals to the principle crystallographic orientations and observations were made with a defocused electron beam. The satellite reflections were extremely weak and long exposure times (up to 80s) were required to record these features; only first order satellites were observed. In general, preferred cleavage favored the location of the [100] zone axis rather [001], although the latter was most informative for direct observation of modulation vectors (Figure 2). Using this procedure, long observation times were possible using a parallel, defocused beam. However, high resolution microscopy was not feasible as more converged electron probes lead to rapid amorphization.
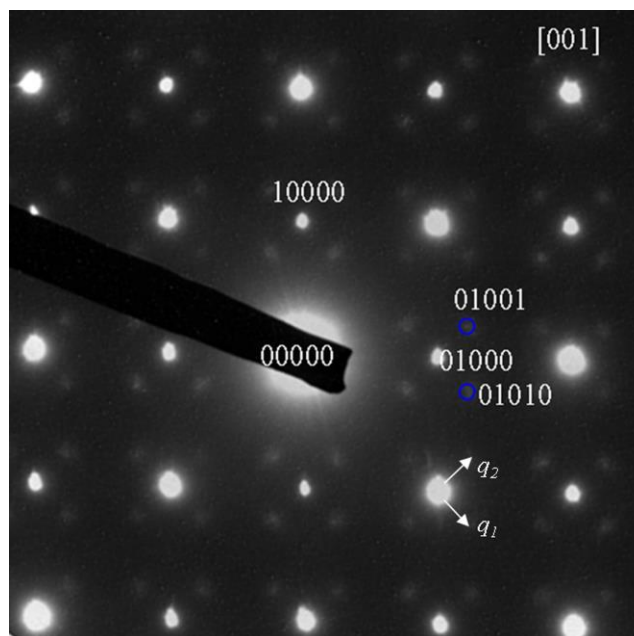
Figure 2. [001] selected area diffraction pattern of $[CaNd]_2[Ga]_2[Ga_2O_7]_2$, showing the q_1 and q_2 modulation.

Results

Crystal Growth: Single crystals up to 5mm in the long dimension were obtained; it was not possible to grow larger crystals due to crack propagation initiated by crystallographic stresses arising from misfit of the tetrahedral network and the interlayer cations. In this respect, it is noted that single crystals with larger interlayer species (e.g. Sr rather Ca) were easily obtained even with very a high growth speed (10mm/h); the structural details of the commensurate Sr-melilites that conform to $P\bar{4}2_1m$ will be reported elsewhere.

Powder X-ray Diffraction: Rietveld refinement of the average structure confirmed single phase melilite, with no evidence of secondary byproducts (Figure 1). The resultant isotropic ADPs are 0.67(3)Å for Nd/Ca, 0.66(3)Å for Ga, and 3.05(18)Å for oxygen

(Table 1), with the latter a probable indication of modulation, but as no satellite reflections were observed, detailed examination was not attempted.

Table 1. Atomic coordinates and isotropic ADP from PXRD for the $P\bar{4}2_1m$ average structure of $[CaNd]_2[Ga]_2[Ga_2O_7]_2$

atoms	x	y	z	occupancy	*Biso*
Ca^I	0.16081(14)	0.66081(14)	0.49232(3)	0.5	0.666(3)
Nd^I	0.16081(14)	0.66081(14)	0.49232(3)	0.5	0.666(3)
Ga^I	0	0	0	1	0.658(3)
Ga^{II}	0.35730(18)	0.85730(18)	0.03628(3)	1	0.658(3)
O^1	0.5	0	0.1928(2)	1	3.05(18)
O^2	0.3555(10)	0.8555(10)	-0.3126(12)	1	3.05(18)
O^3	-0.1634(10)	0.09030(19)	0.2134(11)	1	3.05(18)

Single Crystal X-ray Diffraction: As a two-dimensionally modulated structure, all reflections for $[CaNd]_2[Ga]_2[Ga_2O_7]_2$, were indexed using five integers (*h k l m n*): $\mathbf{H} = h\mathbf{a}^* + k\mathbf{b}^* + l\mathbf{c}^* + m\mathbf{q}_1 + n\mathbf{q}_2$, where $\mathbf{a}^*$, $\mathbf{b}^*$ and $\mathbf{c}^*$ are the reciprocal lattice vectors. The modulation vectors $\mathbf{q}_1 = 0.2319(2)$ ($\mathbf{a}^* + \mathbf{b}^*$), $\mathbf{q}_2 = 0.2319(2)$ ($-\mathbf{a}^* + \mathbf{b}^*$) were determined by 637 main reflections and 1891 satellites reflections. Experimental and refinement details are collected in Table 2.

Table 2
Experimental details

Crystal data	
Chemical formula	$CaNdGa_3O_7$
Chemical formula weight	505.47
Temperature (K)	293
Cell Setting	Tetragonal
Superspace group	$P\bar{4}2_1m(\alpha,\alpha,0)00s(\bar{\alpha},\alpha,0)000$
a (Å)	7.8868(4)
c (Å)	5.2243(3)
Volume (Å^3)	324.96(4)
Formula units (Z)	2

D_x (Mg m^{-3})	5.139
Modulation wave vectors	$\boldsymbol{q}_1 = 0.2319(2)\,(\boldsymbol{a}^* + \boldsymbol{b}^*)$
	$\boldsymbol{q}_2 = 0.2319(2)\,(-\boldsymbol{a}^* + \boldsymbol{b}^*)$
Crystal form	Irregular
Crystal size (mm)	$0.10 \times 0.08 \times 0.15$
Crystal colour	Purple under sunlight
	Blue under fluorescent lamp
Data collection	
Diffractometer	Bruker Smart ApexII Four circle diffractometer
Radiation type	Mo $K\alpha$
Wavelength (Å)	0.71073
Absorption correction type	Multi-scan
Absorption coefficient μ (mm^{-1})	20.777
Range of h, k, l, m, n	$-12 \to h \to 9$
	$-12 \to k \to 9$
	$-7 \to l \to 5$
	$-1 \to m \to 1$
	$-1 \to n \to 1$
No. of measured reflections	17097
No. of unique reflections	5249
No. of observed reflections	2219
No. of main reflections	637
No. of satellites	
For $\pm(1, 0) \pm(0, 1)$	1531
For $\pm(1, 1) \pm(-1, 1)$	51
Criterion for observed reflections	$I > 3\sigma(I)$
Refinement	
Refinement on	F
R, wR (all reflections)	0.0378, 0.0519
R, wR (main reflections)	0.0236, 0.0316
R, wR (satellites) for $\pm(1, 0) \pm(0, 1)$	0.0645, 0.0721
For $\pm(1, 1) \pm(-1, 1)$	0.1690, 0.1567
S	2.20
No. of parameters	322
Weighting scheme	$w = [\sigma^2(F) + (0.01F)^2]^{-1}$
$(\Delta/\text{s.u.})_{max}$	0.0195
$\Delta\rho_{max}$ (e Å^{-3})	1.41
$\Delta\rho_{min}$ (e Å^{-3})	-1.23
Extinction correction	B-C type 1 Lorentzian isotropic (Becker & Coppens, 1974)
Extinction coefficient	4600(300)
Source of atomic scattering factors	International Tables for Crystallography (1992, Vol.C)[31]

Selected Area Diffraction Pattern: The [001] pattern was composed of the main reflections and first order satellites that can be indexed by five integers, $\mathbf{H} = h\mathbf{a}^* + k\mathbf{b}^* + l\mathbf{c}^* + m\mathbf{q}_1 + n\mathbf{q}_2$ (Figure 2). The first order satellites form a square around the principle reflections, consistent with tetragonal symmetry. The modulation vectors $\mathbf{q}_1^s = 0.234\ (\mathbf{a}^* + \mathbf{b}^*)$, $\mathbf{q}_2^s = 0.234(-\mathbf{a}^* + \mathbf{b}^*)$, are in good agreement to those obtained by single crystal X-ray diffraction.

Superspace Group Description: The five-dimensional incommensurate structure can be visualized as a 3-dimensional physical object combined with 2 higher dimensions. The corresponding superspace group contains the symmetry of the basic structure, plus the symmetry elements in the higher dimension, and for melilite, the superspace group symbol $P_{p4mg}^{P\bar{4}2_1m}$ (notation according to Janner *et al.*[32]) was adopted; a comprehensive explanation of this terminology is given by Bindi *et al.*[33] The upper terms refer to the basic structure, with the lower part representing the respective higher dimensional symmetry operations. For example, the $\bar{4}$ superscript directly above the 4 subscript means there is 4-fold inversion in physical space and 4-fold rotation in the higher dimension; 2_1 over m indicates a mirror plane in addition to the screw axis in the 3D space; while the last pair shows a glide related to the mirror symmetry m.

Stokes *et al.*[34] have recently derived all the (3+2) superspace groups, and suggested an extended formalization. Accordingly, $[CaNd]_2[Ga]_2[Ga_2O_7]_2$ adopts the melilite basic metric $a = 7.8868(4)$, $c = 5.2243(3)$Å with two incommensurate modulation vectors: $q_1 = 0.2319(2)(\mathbf{a}^*+\mathbf{b}^*)$, $q_2 = 0.2319(2)(-\mathbf{a}^*+\mathbf{b}^*)$, resulting in a superspace group $P\bar{4}2_1m(\alpha,\alpha,0)00s(\bar{\alpha},\alpha,0)000$, where $\alpha = 0.2319(2)$ is the magnitude of

modulation vectors, and $s = 1/2$ indicates an intrinsic translation, which corresponds to the glide plane in the notation of Janner.[32]

Refinement of Single Crystal XRD Data: The average structure in physical space was refined using the 637 main reflections with $I > 3\sigma(I)$, and quickly converged to $R_{obs}^{all} = 0.0297$, with the composition $[Ca_{1.023(3)}Na_{0.977(3)}]_2[Ga]_2[Ga_2O_7]_2$, that is close to the notional $[CaNd]_2[Ga]_2[Ga_2O_7]_2$. Table 3 lists the refined atomic coordinates and anisotropic displacement parameters for the average structure. To refine the 5D structure, modulation of both atomic position and displacement parameters were applied using the satellite reflections (1, 0), (0, 1), (1, 1), and (-1, 1). The number of observed (1,1) and (1,-1) satellites was found to be very low due to the fact that $\alpha \sim 1/4$, and the 2nd order satellites $(h, k, l, 1, 1)$, $(h+1, k, l, -1, 1)$, $(h, k, l, 1, -1)$ $(h, k+1, l, -1, -1)$ cannot be separated, leading to a relatively high R_{obs}^{2nd} factor (~0.17) for 2nd order satellites. Overlap correction was applied during the refinement by treating pairs of combined satellites as fully overlapped reflections. Separate refinements of 1st and 2nd order satellites were performed, and inclusion of the small number of observed 2nd order satellites, together with 1st order satellites lowered R_{obs} factors, especially R_{obs}^{1st} by about 12% (0.072 to 0.064). Nd/Ca also exhibit occupational modulations, leading to a significant R_{obs}^{all} reduction (0.049 to 0.036).

Table 3. Atomic coordinates and anisotropic displacement parameters for average structure

Atoms			x	y	z	$Occu$	$Uiso$
Nd[1]	4e	..m	0.15917(5)	0.65917(5)	0.49516(10)	0.489(4)	0.01327(15)
Ca[1]	4e	..m	0.15917(5)	0.65917(5)	0.49516(10)	0.511(4)	0.01327(15)

Ga^I	2a	-4..	0	0	0	1	0.0112(2)
Ga^{II}	4e	..m	0.35651(7)	0.85651(7)	0.03522(14)	1	0.00910(15)
O^1	4e	..m	0.3599(5)	0.8599(5)	-0.3063(10)	1	0.0210(11)
O^2	2c	2.mm	0.5	1	0.1990(15)	1	0.033(2)
O^3	8f	1	-0.1622(6)	0.0904(12)	0.2082(9)	1	0.049(2)

Atoms	U_{11}	U_{22}	U_{33}	U_{12}	U_{13}	U_{23}
Nd^1	0.0162(2)	0.0162(2)	0.0073(3)	-0.00759(17)	-0.00014(12)	-0.00014(12)
Ca^1	0.0162(2)	0.0162(2)	0.0073(3)	-0.00759(17)	-0.00014(12)	-0.00014(12)
Ga^I	0.0123(3)	0.0123(3)	0.0089(5)	0	0	0
Ga^{II}	0.0106(2)	0.0106(2)	0.0061(3)	0.0013(2)	0.00164(15)	0.00164(15)
O^1	0.0262(18)	0.0262(18)	0.011(2)	-0.013(3)	0.0028(13)	0.0028(13)
O^2	0.048(4)	0.048(4)	0.002(3)	-0.032(5)	0	0
O^3	0.022(2)	0.109(6)	0.0167(19)	0.034(3)	-0.0128(18)	-0.025(3)

Discussion

Average structure

In the average structure, the GaO_4 tetrahedra form pentagonal rings that stack along [001] to create channels. The Nd/Ca cations align as chains inside these channels and are positioned between the layers (Figure 3). The average structure features a strong anisotropy of the Nd/Ca and O displacement ellipsoids; O^2 has the longest ellipsoidal axis directed along $\langle 110 \rangle$. Ga^{II}-O^2-Ga^{II} is linear but the O^2 has a large atomic displacement parameter perpendicular to the Ga^{II}-O^2 vector; this suggests bending of the Ga^{II}-O^2-Ga^{II} bond and the real Ga^{II}-O^2 distance is longer. This observation is consistent with twisting of the $Ga^{II}_2O_7$ tetrahedral dimers around $\langle 001 \rangle$, accommodated by a slight rotation of the Ga^IO_4 tetrahedra, probably also along $\langle 001 \rangle$. O^3 elongates towards the A site atoms, due to the size misfit of the interstices and the Nd/Ca ionic size.
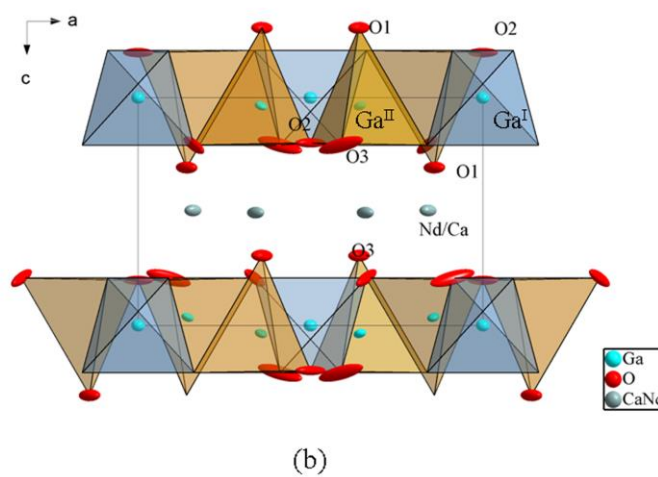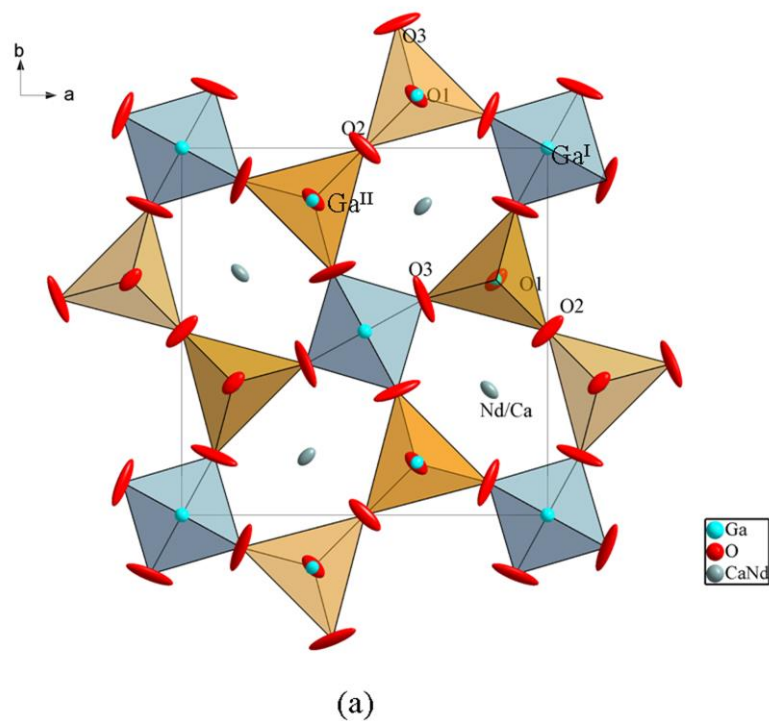
Figure 3. The average structure of $[Ca_2Nd_2][Ga]_2[Ga_2O_7]_2$, obtained through single crystal X-ray diffraction. (a) projected along $\langle 001 \rangle$, and (b) $\langle 010 \rangle$. Atoms are represented by 50% probability displacement ellipsoids.

Modulated Structure

An approximant $4a \times 4a \times 1c$ cell illustrates the modulation (Figure 4). Deformation of the pentagonal rings is clear and gives rise to a change of coordination around the A cations. Six-, seven- and eight-coordinate A cations exist in different parts of the structure, assuming A–O distances > 2.9Å are disregarded. The A–O bonds, especially the longest ones, are strongly influenced by the displacive modulation, whereby lengthening and shortening are imposed in different regions of the crystal, leading to a change in the A site coordination (Figure 5). For example, the largest modulations are observed at the longest bonds A—O^3-v,vii, with a deviation of bond lengths up to 1.18(2)Å, while the second longest bonds A—O3-iv,viii have differences below 0.52(2)Å. Smaller influences are exerted on the shorter A—O^1-i bond; the regular Nd/Ca—O^1-i bond is 2.383(2) Å[35], while the stretched average distances are 2.45(8)Å, varying from 2.37(8)Å to 2.53(8)Å in the modulated structure. Variations of bond distances caused by modulation can be observed as a function of t and u, the additional two-dimensional space coordinates. For instance, in Figure 5, at some regions, the A—O^3 bonds show the greatest variance in excess of 2.9Å, while the strong short bonds A—O^2, and A—O^1 are more constant (Table 4). The A—O bond distributions at t=0, u=0 show that there are 35.9% eight-, 29.6% seven-, and 34.5% six-coordinate A—O polyhedra. Occupational modulation is also found for the A site Nd/Ca atoms; at $u = 0$, the occupancy of Nd varies from 0.518(12) to 0.580(12), while Ca ranges from 0.420(13) to 0.472(13) as a function of t (Figure 7). Nd-rich and Ca-rich areas can be found at different regions of t and u. Areas of strongest polyhedral distortion correspond to a Ca-rich area, where almost all the six-coordinated polyhedra emerge (Figure 4).
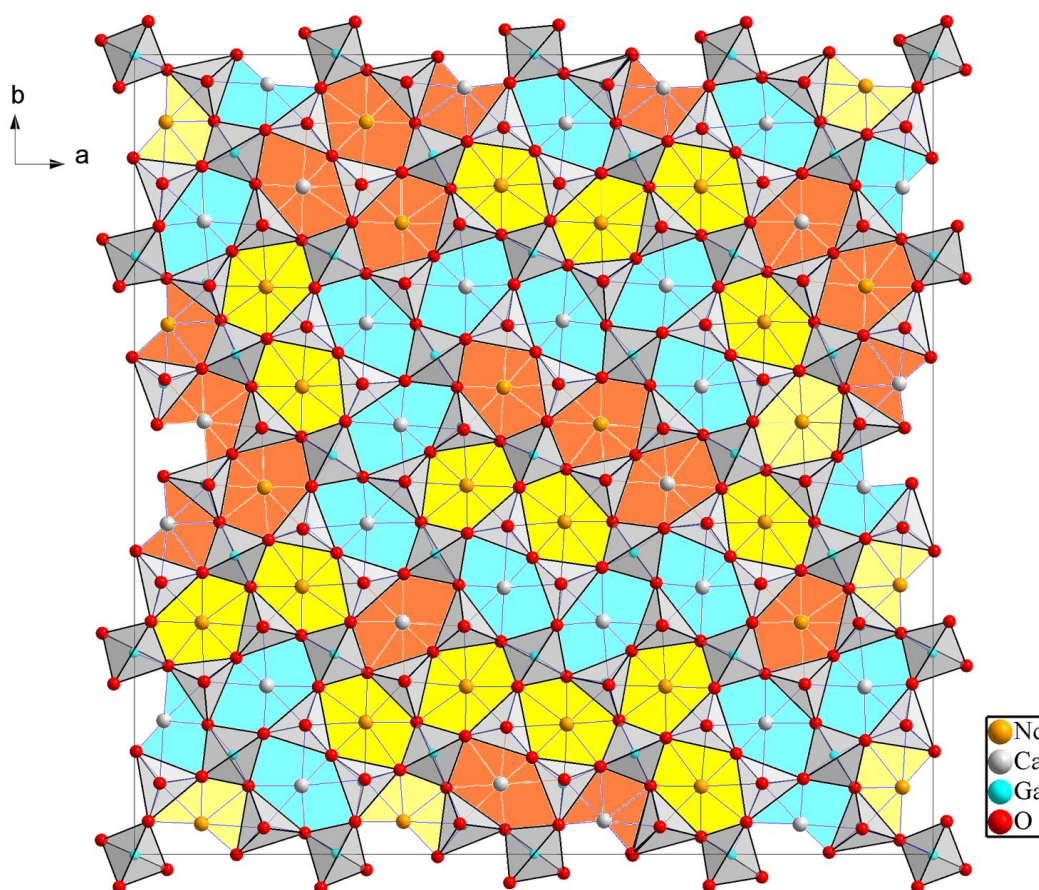
Figure 4. The approximate modulated structure of $4a \times 4a \times 1c$ cell, projected along the c axis. Nd/Ca-O bonds < 2.9 Å are represented by sticks. 6-coordinate Nd/Ca pentagons are highlighted in aqua, 7-coordinate pentagons are orange, and 8-coordinated are yellow. The Ga^IO_4 and $Ga^{II}O_4$ tetrahedra are shown as grey.

Because the interlayer A cations are too small, compared with the space between the layers, the tetrahedral sheets must distort. The strongest distortion occurs for the $Ga^IO^3_4$ tetrahedra (Figure 8), which is compromised by bending of the $Ga^{II}_2O_7$ tetrahedral dimers (Figure 9) to stabilize the structure. Positional disorder is introduced into the structure because of this distortion, and consequently, modulation develops. Smaller A cations give

rise to larger distortions, and therefore the structure is more likely to be incommensurate. For a regular $Ga^IO^3_4$ tetrahedron in the average structure, the Ga-O bond is 1.8242(4) Å; however, the modulation distributes the $Ga^IO^3_4$ bond lengths from 1.68(6) Å to 1.98(6) Å (Table 4). The O^3-Ga^I-O^3 bond angle variations are shown in Figure 10, with the largest deviation from around 21.50(11)° from the regular tetrahedral angle of 109.49°. In the $Ga^{II}O_4$ tetrahedron, the largest distortion occurs for the O^3-iv—Ga^{II}—O^3-viii angle as well as the Ga^{II}-O^3 bonds, with variation of ±17.25(4)° from the average structure (99.246°) and bond length variation of 0.36(12)Å can be found throughout the structure (Figure 11).

Table 4. Modulated structure: Interatomic distances (Å) and tetrahedral angles (°)

	average	minimum	maximum
A-O polyhedra			
O^1-i	2.45(7)	2.37(8)	2.53(8)
O^1-ii	2.58(8)	2.38(8)	2.82(8)
O^1-iv	2.57(8)	2.38(8)	2.83(8)
O^2-i	2.42(5)	2.28(5)	2.56(5)
O^3-iv	2.48(6)	2.24(6)	2.74(6)
O^3-v	2.90(6)	2.42(6)	3.64(6)
O^3-vii	2.90(6)	2.42(6)	3.65(6)
O^3-viii	2.49(6)	2.24(6)	2.76(6)
Ga^IO_4 tetrahedra			
Ga^I-O^3	1.83(6)	1.68(6)	1.98(6)
O^3-i—Ga^I—O^3-ii	110(3)°	90 (2)°	131(3)°
O^3-i—Ga^I—O^3-iv	107(3)°	102(3)°	113(3)°
O^3-i—Ga^I—O^3-v	110(3)°	90(2)°	131(3)°
O^3-ii—Ga^I—O^3-iv	110(3)°	90(2)°	131(3)°
O^3-ii—Ga^I—O^3-v	107(3)°	102(3)°	113(3)°
O^3-iv—Ga^I—O^3-v	110(3)°	90(2)°	131(3)°
$Ga^{II}O_4$ tetrahedra			
Ga^{II}-O^1	1.79(8)	1.72(9)	1.87(9)
Ga^{II}-O^2	1.82(6)	1.77(7)	1.86(5)
Ga^{II}-O^3	1.84(6)	1.69(6)	2.05(6)

O^1-i—Ga^{II}—O^2-i	117(3)°	114(3)°	120(3)°
O^1-i—Ga^{II}—O^3-iv	119(3)°	111(3)°	131(3)°
O^1-i—Ga^{II}—O^3-viii	119(3)°	111(3)°	130(3)°
O^2-i—Ga^{II}—O^3-iv	100(4)°	87(4)°	112(4)°
O^2-i—Ga^{II}—O^3-viii	100(4)°	87(4)°	112(4)°
O^3-iv—Ga^{II}—O^3-viii	97(3)°	82(3)°	110(2)°

Symmetry codes : (i) x, y, z; (ii) y, -x, 1-z ; (iii) x, y, -1+z ; (iv)-x, -y, -1+z ; (v) –y, x, 1-z ;

(vi) x, y, 1+z ; (vii) ½+x, ½-y, 1-z ; (viii) ½-y, ½-x, z ; x, y, z are the average atomic

coordinates in space group $P\bar{4}2_1m$.
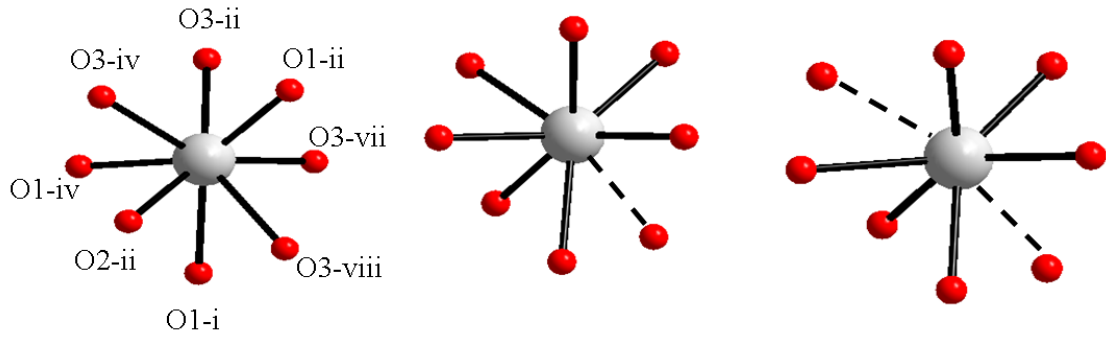
Figure 5. The eight-, seven-, and sixfold coordination of the *A* site cations. Bonds longer

than 2.9Å are represented by dashed lines. The atomic coordinates were at *t*=0, *u*=0;

t=0.5, *u*=0.5; *t*=0.6, *u*=0; respectively. For the symmetry codes refer to Table 4.
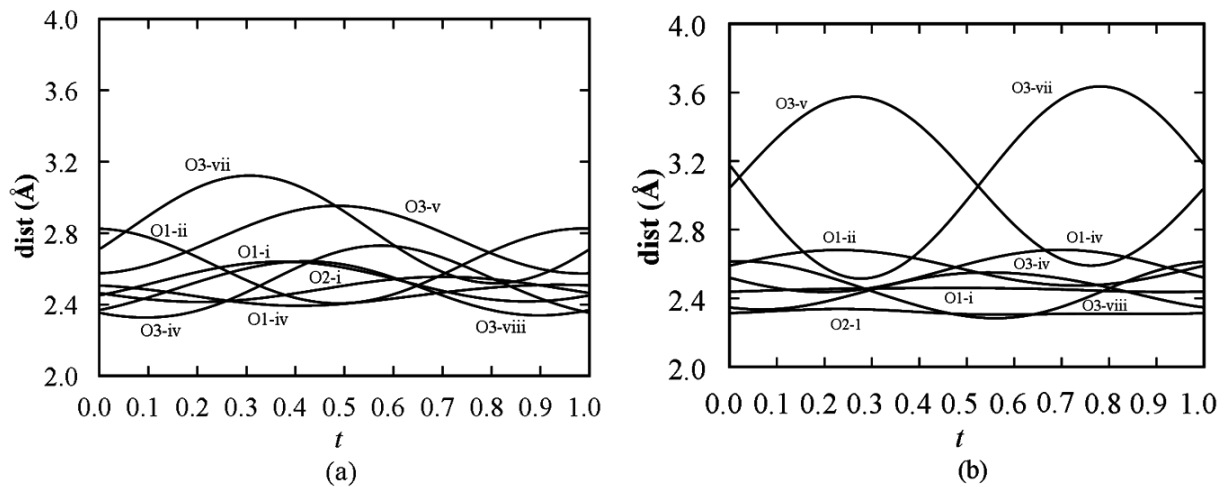
Figure 6. Variation of A-O bond distances as a function of t, at $u = 0$ and $u = 0.610$. At some regions, A-O^3 bonds exceed 2.9Å. Symmetry codes are in Table 4.
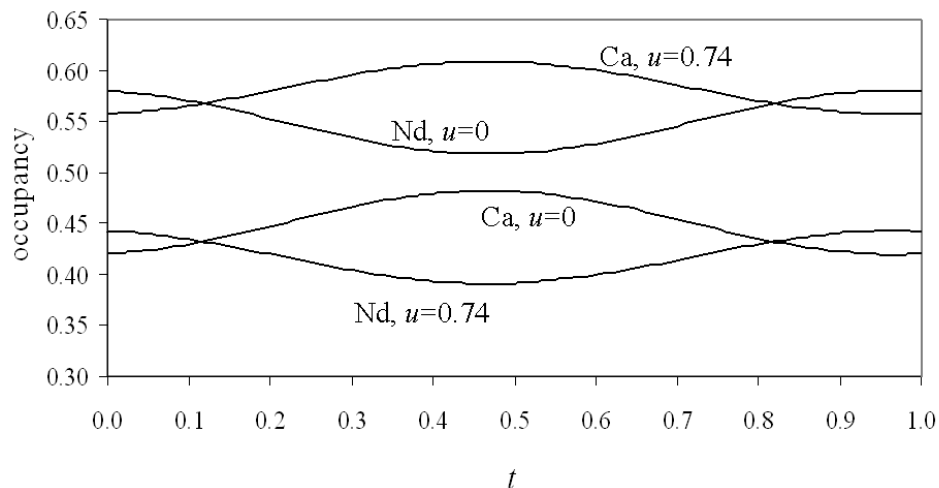
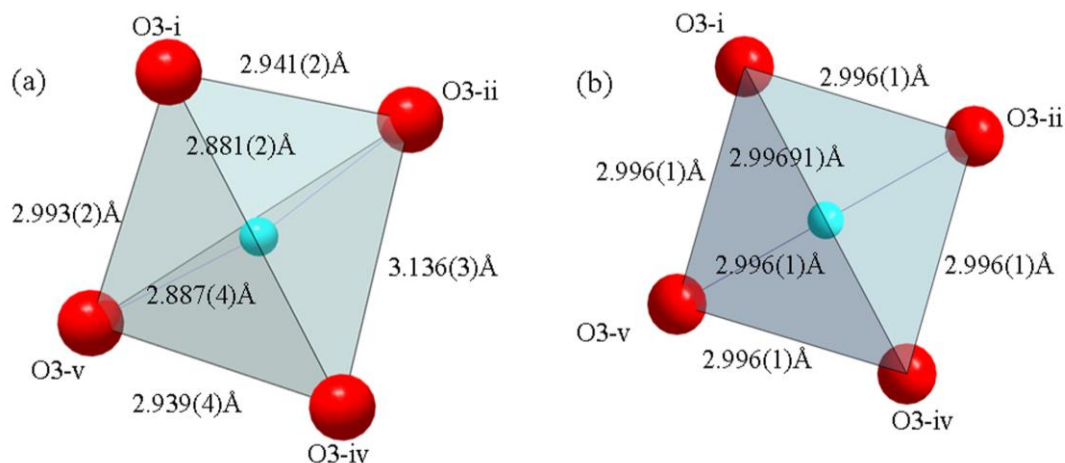**Figure 7.** Occupancy variation for the A site atoms Nd and Ca at different u as a function of t.

Figure 8. (a) Distorted and (b) undistorted Ga^{I}O$^3_4$ tetrahedra, viewed along c axis, (a) is extracted from the approximant $4a \times 4a \times 1c$ cell of the modulated structure. Symmetry codes are shown in Table 4.
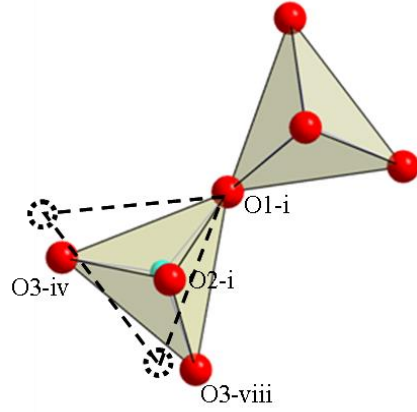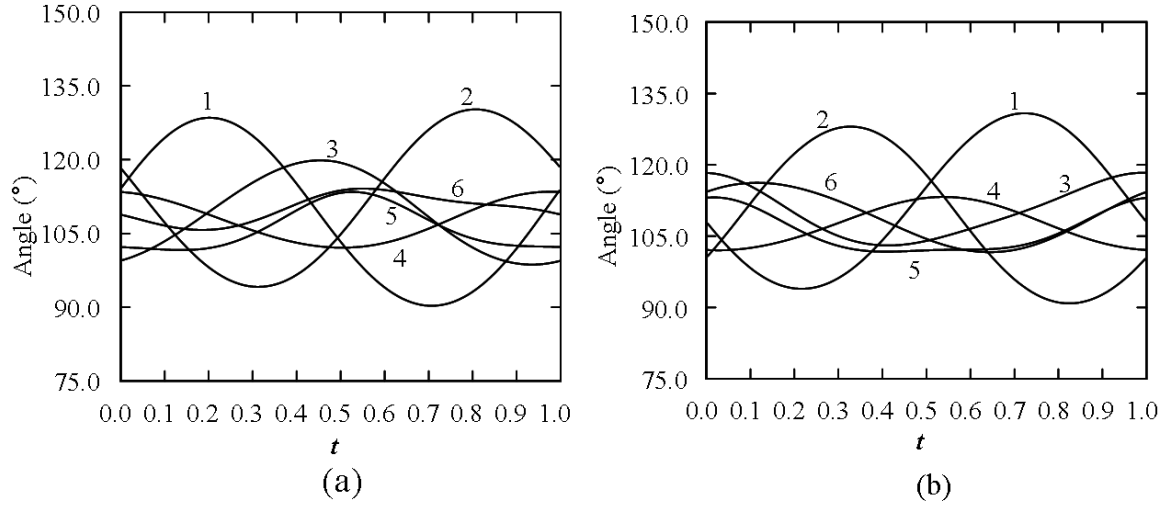
Figure 9. The bent $Ga^{II}_2O_7$ tetrahedral dimmers, dashed lines show the ideal position, viewed along *c* axis. Symmetry codes are listed in Table 4.

1: O^3-ii —Ga^I— O^3-iv   2: O^3-i —Ga^I— O^3-v   3: O^3-iv —Ga^I— O^3-v

4: O^3-i —Ga^I— O^3-iv   5: O^3-ii —Ga^I— O^3-v   6: O^3-i —Ga^I— O^3-ii

Figure 10. Bond angle variations for $Ga^IO^3_4$ tetrahedra at a function of *t*, (a) at *u*=0, (b) *u*=0.5. Symmetry codes are in Table 4.

1: O¹-i—Ga^{II}—O³-iv   2: O¹-i—Ga^{II}—O³-viii   3: O¹-i—Ga^{II}—O²-i

4: O³-iv—Ga^{II}—O³-viii 5: O³-viii—Ga^{II}—O²-i   6: O³-iv—Ga^{II}—O²-i

1:Ga^{II}—O³-iv;   2:Ga^{II}—O³-viii;   3:Ga^{II}—O¹-i;   4:Ga^{II}—O²-i;
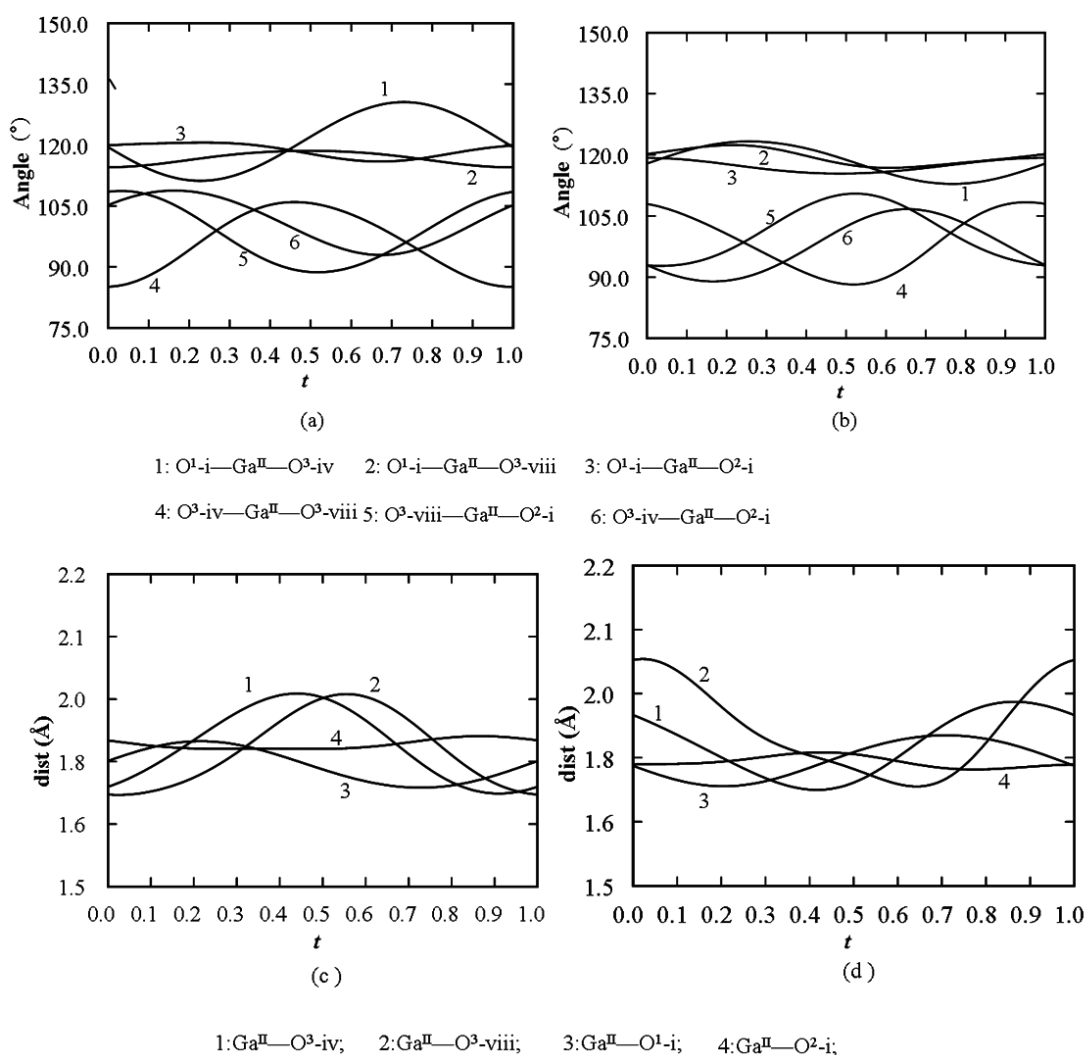
Figure 11. Bond angle (a), (b) and bond length (c), (d) variations for Ga^{II}O$_4$ tetrahedron as a function of t, at (a) (c) u=0, (b) (d) u =0.50. The symmetry codes are the same as in Table 4.

Bond valence summations

The bond valence sums (BVS) for all the cations were calculated in order to evaluate the validity of the structure (Table 5.) The BVS of Nd/Ca were obtained by summing the partial bond valence of Nd and Ca through the occupancy ratios along t and u, using the

21

parameters of Altermatt & Brown[36] (Figure 12). Similar to the reported incommensurate structure $[Ca_2]_2[Co]_2[Si_2O_7]_2$,[21] the values for Nd/Ca are remarkably lower than the formal charges, consistent with the interstices being too large for the A site cations. High BVS regions correspond to the areas with Nd occupancy dominant, probably because of the larger affinity of Nd^{3+} ions to oxygen. The BVS values for Ga^I and Ga^{II} show large variations, but their mean values are within a tolerable range. In fact, aside from the remarkable variation, the mean values of BVS for all cations in the modulated structure are closer to the formal values than those calculated for the average structure (Table 5).

Table 5. Bond Valence Sums

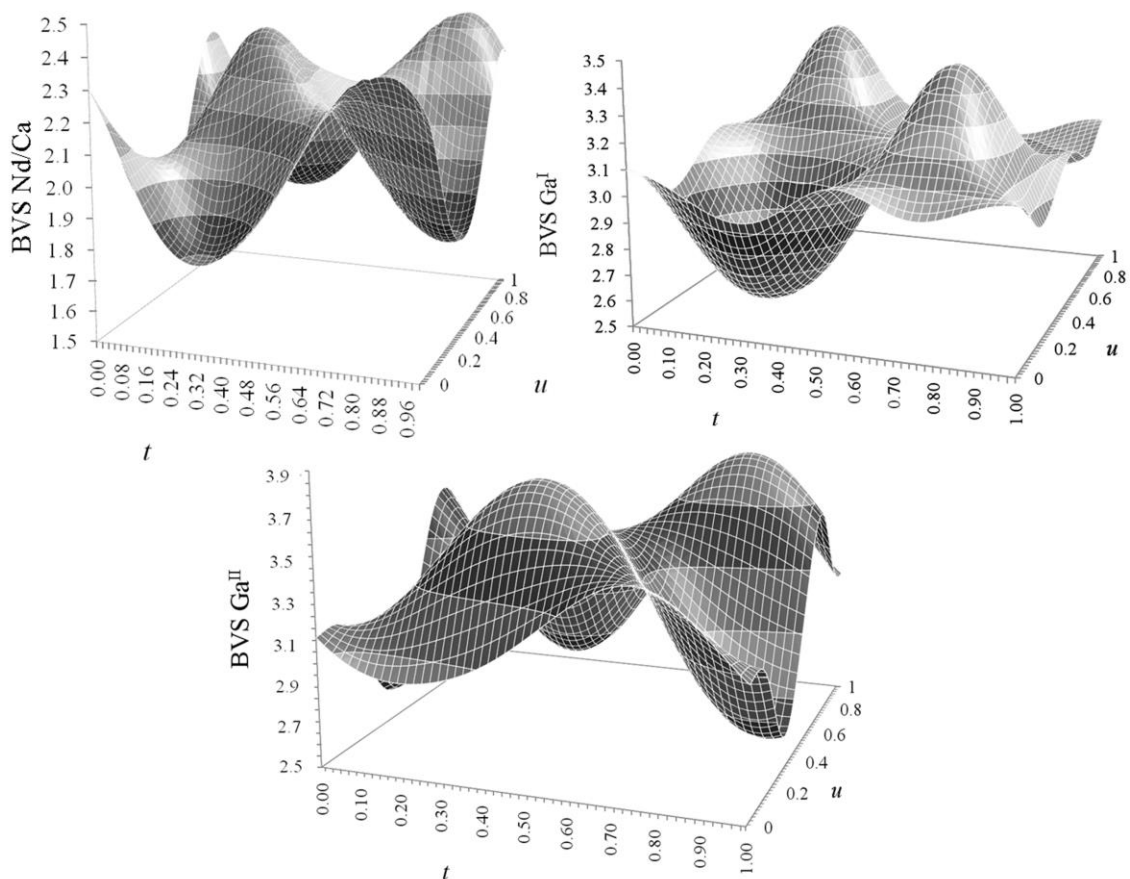|			Modulated structure		
	Formal value	Average structure	Mean value	Minimum	Maximum
Nd/Ca	2.5	2.02(10)	2.09(12)	1.79(3)	2.44(3)
Ga^I	3	3.14(2)	3.09(3)	2.94(10)	3.56(10)
Ga^{II}	3	3.21(2)	3.15(11)	2.62(10)	3.69(3)

Figure 12. Bond valence sum (BVS) variations for *A* site atoms as a function of *t* and *u*. BVS was calculated according to the ratio of Nd/Ca at different *t* and *u*.

Modulation vectors

While the number of fully determined modulated melilite structures remains quite small, sufficient data is now available to search for crystallochemical correlations. The value of α for q_1 and q_2 can be related to chemical composition, particularly the *A/B* ionic radius ratio (Figure 13). Cation substitutions at the different sites are found to have distinct effects on the modulation vector. For example, substitutions of larger ions at the *B* site leads to an increase in α, while similar substitutions at the *A* site generally induce the opposite effect, e.g. in $[Ca_2]_2[Fe_xMg_{1-x}]_2[Si_2O_7]_2$[37] increasing the Fe content

$(r(Fe^{2+})>r(Mg^{2+}))$ causes α to increase, while α decreases when Sr content increases in $[Ca_{1-x}Sr_x]_2[Mg]_2[Si_2O_7]_2$[38] and $[Ca_{1-x}Sr_x]_2[Co]_2[Si_2O_7]_2$[21] $(r(Sr^{2+})>r(Ca^{2+}))$. Both situations accommodate increasing α when the A/B ratio decreases, which results in less structural distortion. However, some melilite compositional joins do not always obey the same trend, indicating that along with the A/B size ratio, different charge combinations for species occupying the same crystallographic site are also important. For example, it is seen that α increases along with A/B ratio when 4% of Ca is replaced by Sr in $[Ca_2]_2[Mg]_2[Si_2O_7]_2$,[20] and this may reflect ordering of the A cations. Similarly, for $[CaNd]_2[Ga]_2[Ga_2O_7]_2$ and $[CaLa]_2[Ga]_2[Ga_2O_7]_2$ enhanced ordering expected for the latter because the larger cation size difference, will give a larger α. In another example, the tetrahedral size deviation of ZnO_4 and GeO_4 is probably responsible for the abrupt α discontinuity of $[Ca]_2[Zn]_2[Ge_2O_7]_2$. In this review of melilite modulation, the only case that cannot be explained by these systematics is for $[Ca_2]_2[Mg]_2[Si_2O_7]_2$-$[Ca_2]_2[Co]_2[Si_2O_7]_2$, where the Co^{2+} (0.56Å) ionic radius is slightly smaller than Mg^{2+}(0.57Å),[35] but α is significantly larger. Possibly, crystal field effects for Co^{2+} account for this apparent anomaly. Moreover, at room temperature $[Ca_2]_2[Mg]_2[Si_2O_7]_2$ is close to its incommensurate-commensurate phase transition temperature (~80°C), and the abrupt decrease in α may precede the onset of this transformation.[39] It is notable that for the related $[A_2]_2[B]_2[M_2O_8]_2$ fresnoite materials similar trends have not yet established. It is suggested this may be due to the prevalence of nanoscale intergrowths of commensurate and incommensurate domains which mask simple correlations between α and compositions.[40]
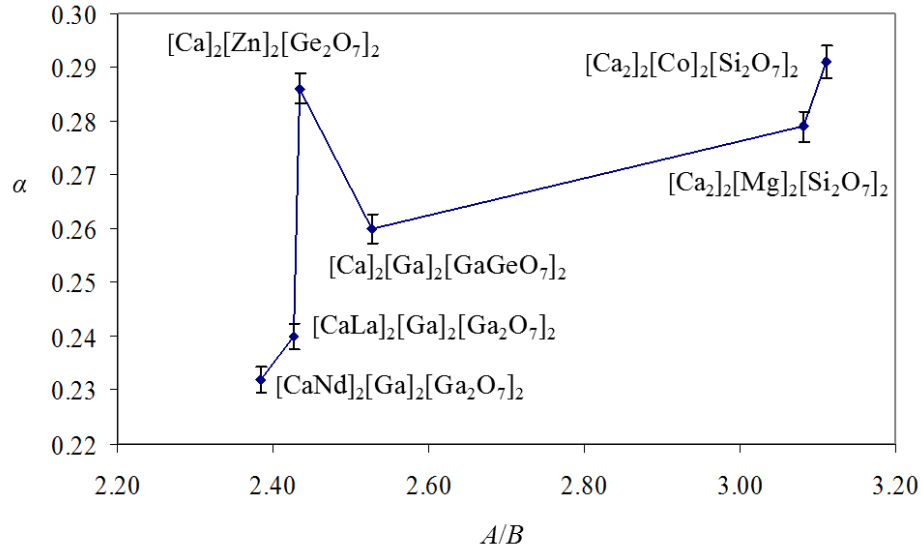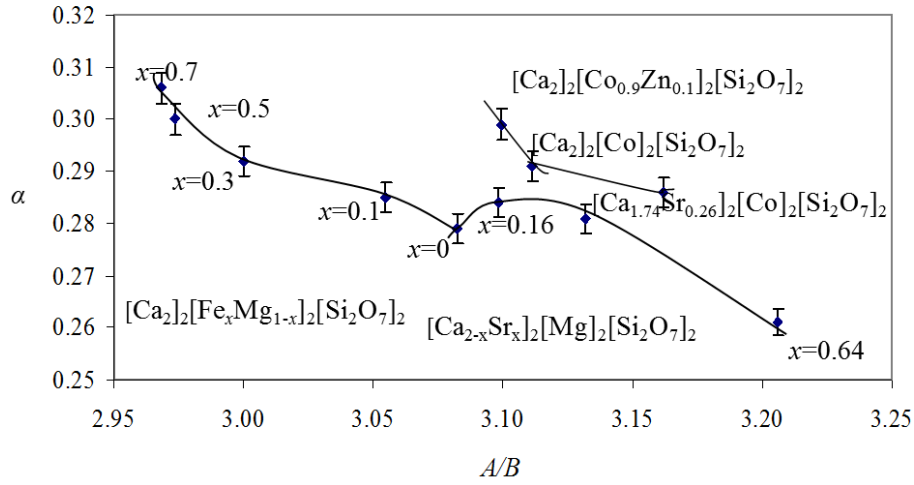
Figure 13. Relationship of α with cation ratio A/B: (a) for end member compositions, (b) for cation substitutions at A or B sites. Ionic radii of B site cations are calculated according to their respective ratio. The α for $[Ca_2]_2[Fe_xMg_{01-x}]_2[Si_2O_7]_2$ is re-calculated from the Seifert *et al.*;[37] with $[Ca_2]_2[Co_{0.9}Zn_{0.1}]_2[Si_2O_7]_2$ from Jia. *et al.*;[38] $[Ca_{2-x}Sr_x]_2[Co]_2[Si_2O_7]_2$ from Bagautdinov *et al.*[21] and $[Ca_{2-x}Sr_x]_2[Mg]_2[Si_2O_7]_2$ from Jiang *et al.*[20] $[CaLa]_2[Ga]_2[Ga_2O_7]_2$ and $[Ca_2]_2[Ga]_2[GaGeO_7]_2$ are obtained from SAED (see Figure 14).

$[CaLa]_2[Ga]_2[Ga_2O_7]_2$
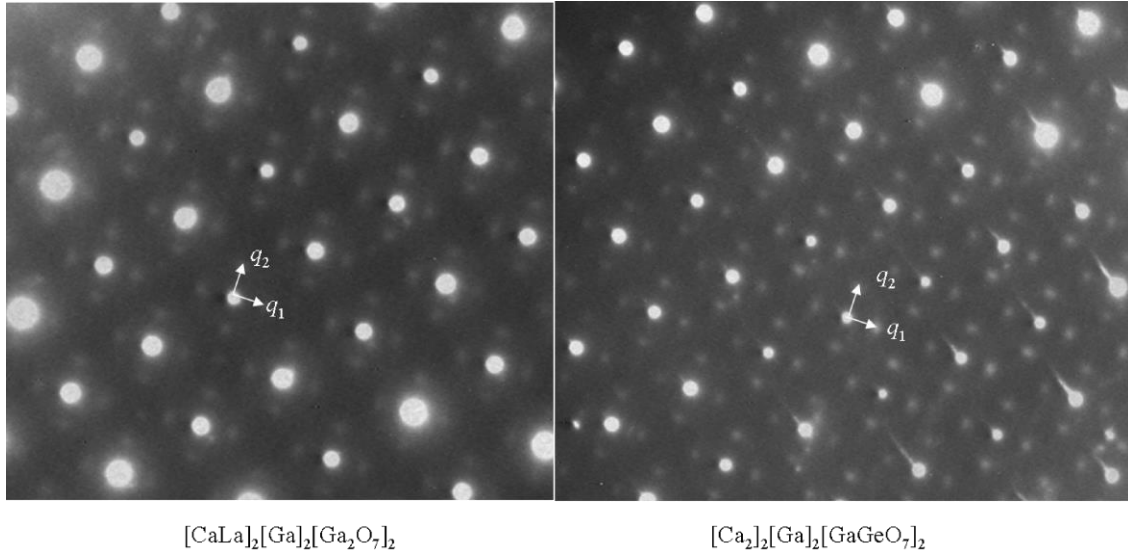
$[Ca_2]_2[Ga]_2[GaGeO_7]_2$

Figure 14. SAED for $[CaLa]_2[Ga]_2[Ga_2O_7]_2$ and $[Ca_2]_2[Ga]_2[GaGeO_7]_2$, showing that the modulation vectors of ~0.24 and ~0.26 respectively.

The existence of eight-, seven- and six-coordinated *A* site polyhedra is a distinct feature of the $[CaNd]_2[Ga]_2[Ga_2O_7]_2$ incommensurate structure. Strong distortions of the Ga-O tetrahedra are induced by the variation of interatomic distances. As the incommensurate modulation is due to the misfit between the tetrahedral layers and the size of interlayer cations, smaller *A*-site cations with respect to the *B*-tetrahedra, give rise to greater structural misfit resulting in incommensurate structures and the internal strain that makes the growth of appreciable single crystals more difficult. Therefore, modulation is predicted when Nd/Ca is substituted with smaller lanthanides such as Sm and Gd, or if a larger metalloid enters the *B*-site (e.g. Mg).
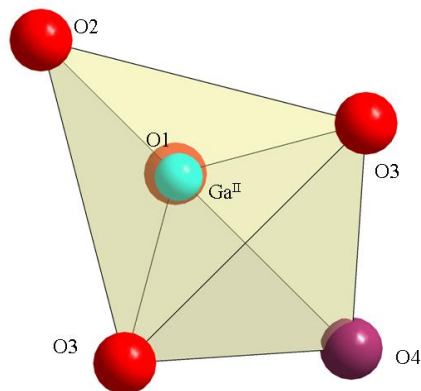
Figure 15. Distorted trigonal bi-pyramidal $Ga^{II}O_5$, O4 represents the interstitial oxygen, viewed along *c* direction. This graph was adopted from Kuang *et al*..[5]

Preferred diffusion pathways

The preferred crystallochemical formula is $[Ca_{1-x}Nd_{1+x}]_2[Ga]_2[Ga_2O_{7+x/2}]_2$ as this provides insight into the location of interstitial oxygen. A greater concentration of Nd than Ca (i.e. Nd/Ca>1) leads to the introduction of mobile oxygen interstitials that fill the pentagonal rings of the tetrahedral layer. The Ga^IO_4 tetrahedron is connected via all four oxygen ions to tetrahedral dimers, while the $Ga^{II}O_4$ tetrahedron contains the non-bridging oxygen O^1 that provides the flexibility to accommodate interstitials through the repositioning of the O^1 to enter the coordination environment of the Ga^{II} resulting in a distorted trigonal bi-pyramidal $Ga^{II}O_5$ polyhedron (Figure 15).[5] Stabilization of interstitial oxygen requires dynamical deformation of the framework that is an important feature of the modulated structure. Large cations at the *A* site can readily accommodate the change of coordination number, and the corner-connected gallium oxide tetrahedral network can stabilize the interstitial oxygen by binding them into the polyhedral network. The preferred interstitial migration path along O^2 and O^3 is shown as oxygen ellipsoid

elongation and excess electron density (Figure 16). Members of the flexible layered-structure melilite family can readily accommodate mobile interstitial oxygen.
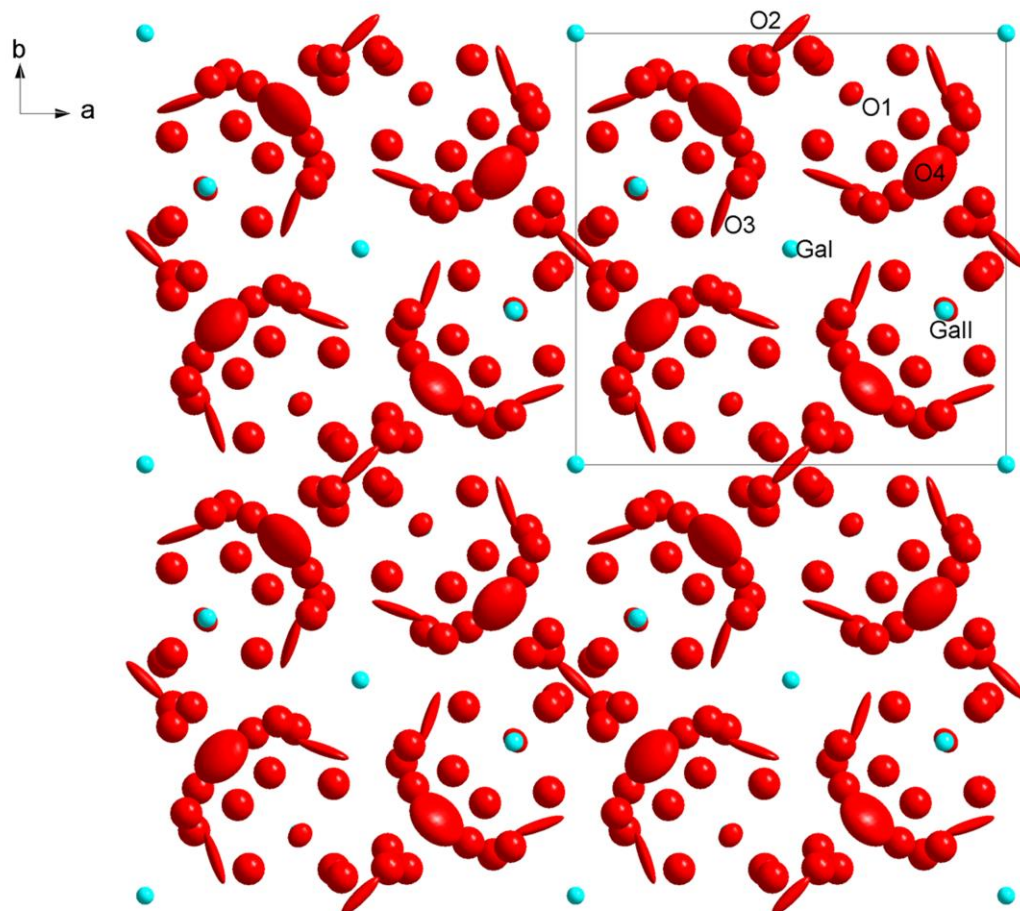

Figure 16. Interstitial oxygen preferred migration path along O^2 and O^3, with no excess electron density indicating migration involving O^1. Fourier peaks are included in the form of oxygen in this representation and are shown in red. The structural representation was derived from a single crystal X-ray diffraction refinement of $[Ca_{0.5}Nd_{1.5}]_2[Ga]_2[Ga_2O_{7.25}]_2$.
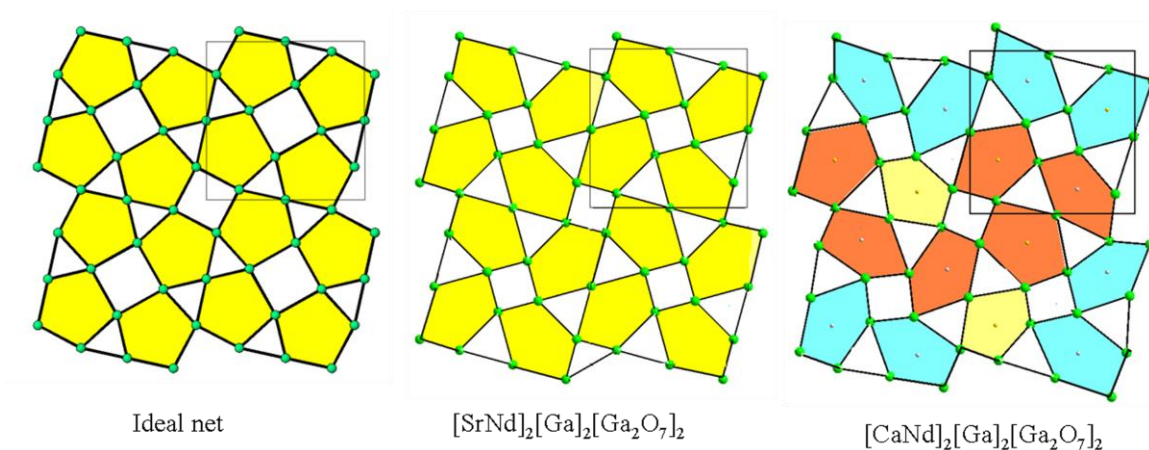
Figure 17. Projected topologies of the $[(3.5.4.5)^2, 3.5.3.5]$ tetrahedron-pentagon oxygen nets of melilite. The ideal net is from O'Keeffe and Hyde,[14] $[SrNd]_2[Ga]_2[Ga_2O_7]_2$ is a commensurate derivative and $[CaNd]_2[Ga]_2[Ga_2O_7]_2$ is modulated. Obvious pentagon distortion can be observed in both non-modulated and modulated nets. 6-, 7- and 8-coordinated polyhedra are filled by aqua, orange and yellow colors, respectively.

Conclusion

Melilites contain a 2D tetrahedral network with pentagons that are distorted even in the non-modulated structures (e.g. $[SrNd]_2[Ga]_2[Ga_2O_7]_2$), but most evidently in the incommensurate form of $[CaNd]_2[Ga]_2[Ga_2O_7]_2$ (Figure 17). This long range distortion enables the flexible deformation which is prerequisite for high interstitial oxygen mobility. Network systematics may be a powerful tool to predict modulation, and also identify compounds as potential low temperature ion conductors. Similar structures containing triangle-quadrangle-pentagon nets include (1) the $[(3.5.4.5)^2, 3.5.3.5]$ net as found for $Ca_5Al_6O_{18}$[41] and fresnoite-types (such as $Ba_2TiSi_2O_8$,[42] $K_2MoAs_2O_9$[43] and $K_2V_3O_8$[44]) that contain pentagons formed from alternate connections of tetrahedral dimers with pyramids TiO_5 (or Mo/VO_5), (2) the $[5.4^3, 5.4.3.4, 5.4^3, (5.4.3.4)^2]$ net as in

$K_3W_5O_{15}$,[14] where 5 corner-connected tetrahedra form pentagon-triangles, with other tetrahedra edge-shared to form the extended network, (3) the $[(5^3.3)^2, 5^3, 5^3.3, 5^3]$ net for hexagonal structures such as $K_3V_5O_{14}$[45] and $CaTa_4O_{11}$,[46] (4) the $[(3.4.5.4)^2, (3.5.4.5)^2]$ net such as $Ba_3Si_4Ta_6O_{26}$ and $Ba_3Si_4Ta_6O_{23}$,[47] where all tetrahedra are corner-connected, (5) the $[3.5.3.5, (3.4.5^2)^2]$ net, e.g. Ta_2O_5,[48] and (6) the $[3.5.3.5, (3.4.5^2)^2]$ net, as in UVO_5[49] (see Table 6). The connected pentagons are likely to provide favorable diffusion pathways for oxygen (Figure 18).[14] Other tetrahedral network candidates include one dimensional net such as Na_2SiO_3[50] and La_2TiO_5[51], two dimensional nets including $LaSrGaO_5$,[52] $Ba_2CuSi_2O_7$,[53] $Na_2Si_2O_5$,[54] $BaSi_2O_5$[55] and nordite $LaSrNa_3ZnSi_6O_{17}$,[56] and three dimensional nets as found in langasite $La_3Ga_5SiO_{14}$[57] where a 2-dimenional tetrahedral net is connected through octahedra.

Table 6. Planar pentagonal nets with the highest proportion of pentagons may be especially suitable for ion conduction.

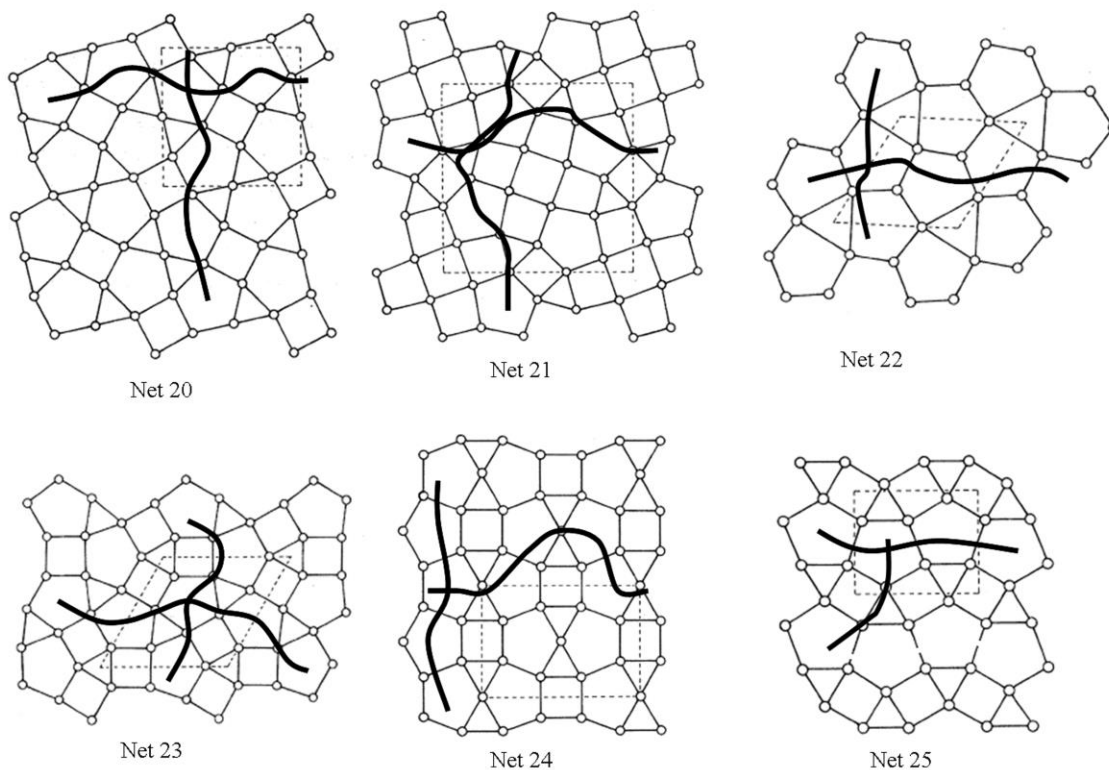| Net[14]	Vertices	% pentagon/quadrangle/triangle	Examples
20	$[(3.5.4.5)^2, 3.5.3.5]$	40/20/40	melilite, fresnoite, $Ca_5Al_6O_{18}$[41]
21	$[5.4^3, 5.4.3.4, 5.4^3, (5.4.3.4)^2]$	20/60/20	$K_3W_5O_{15}$[14],
22	$[(5^3.3)^2, 5^3, 5^3.3, 5^3]$	66.7/0/33.3	$K_3V_5O_{14}$[45], $CaTa_4O_{11}$[46]
23	$[(3.4.5.4)^2, (3.5.4.5)^2]$	33.3/33.3/33.3	$Ba_3Si_4Ta_6O_{26}$ and $Ba_3Si_4Ta_6O_{23}$[47]
24	$[3.5.3.5, (3.4.5^2)^2]$	50/25/25	Ta_2O_5[48]
25	$[3.4.5.4, (3.4.5^2)^2]$	33.3/33.3/33.3	UVO_5[49]

Figure 18. Ideal triangle-quadrangle-pentagon nets with lines showing likely preferred ion diffusion paths.

In the present case, non-bridging oxygen O^1 in the $Ga^{II}O_4$ serves as a key for the interstitial stabilization and mobility in melilite, and in general modulated structures with terminal oxygen and a distorted network are potential candidates for high oxide mobility. Many well-known oxide ion conductors such as fresnoite[58] and fergusonite (e.g.$CeNbO_{4+x}$)[12] are all layered structures. $Ba_{18}Al_{12}O_{36}$[41] also has tetrahedra containing terminal oxygen. One other possible electrolyte is the bismuth calcium aluminate $Bi_2Ca_6Al_{12}O_{27}$[59] where corner-connected AlO_4 tetrahedra form corrugated six- and three-membered rings, edge-sharing with CaO_8 polyhedra aligned along *c* that create three-dimensional nets, with Bi located in large hexagonal tunnels parallel to *c* to form

31

Bi_2O_3 pairs. Another target ceramic may be $Na_2Si_3O_7$[60] that is a (3+1) dimensional incommensurate structure with distorted silicate tetrahedral layers connected by Na. Certain brownmillerites (e.g. $Ca_2Fe_2O_5$)[61] are also incommensurate structures with distorted tetrahedral chains that are ready to accommodate interstitials. Moreover, further reduction of brownmillerites can form infinite-layer oxides (Sr/CaFeO$_2$) with square-planar oxygen coordination that have very high oxygen mobility.[62, 63] Material families sharing these key crystal chemical features with melilite are potential fast oxide ion conductors.

Supporting information available: The CIF for average and modulated structure $[CaNd]_2[Ga]_2[Ga_2O_7]_2$. This material is available free of charge via the Internet at http://pubs.asc.org.

Author Information

Corresponding Author

*Division of Materials Science & Engineering, Nanyang Technological University, Singapore. Email: tbaikie@ntu.edu.sg

Reference

1.	Minh, N. Q., Ceramic fuel-cells. *J. Am. Ceram. Soc* **1993,** 76, (3), 563-588.
2.	Goodenough, J. B., Oxide-ion conductors by design. *Nature* **1999,** 404, 821-822.
3.	León-Reina, L.; Losilla, E. R.; Martinez-Lara, M.; Bruque, S.; Aranda, M. A. G., Interstitial oxygen conduction in lanthanum oxy-apatite electrolytes. *J. Mater. Chem.* **2004,** 14, 1142-1149.
4.	Packer, R. J.; Tsipis, E. V.; Munnings, C. N.; Kharton, V. V.; Skinner, S. J.; Frade, J. R., Diffusion and conductivity properties of cerium niobate. *Solid State Ionics* **2006,** 177, 2059-2064.
5.	Kuang, X. J.; Green, M. A.; Niu, H. H.; Zajdel, P.; Dickinson, C.; Claridge, J. B.; Jantsky, L.; Rosseinsky, M. J., Interstitial oxide ion conductivity in the layered tetrahedral network melilite structure. *Nature Mater.* **2008,** 7, 498-504.
6.	Raj, E. S.; Skinner, S. J.; Kilner, J. A., Electrical conductivity, oxygen diffusion and surface exchange studies on a melilite-type $La_{1.05}Sr_{0.95}Ga_3O_{7+zelta}$. *Solid State Ionics* **2005,** 176, 1097 - 1101.
7.	van Smaalen, S., *Incommensurate crystallography*. Oxford University Press: New York, 2007.
8.	de Pater, C. J.; Helmholdt, R. B., Incommensurate structural phase transformation in Na_2CO_3. *Phys.Rev.B* **1979,** 19, (11), 10.
9.	Boudard, M.; de Boissiu, M.; Janot, C.; Heger, G.; Beeli, C.; Nissen, H. U.; Vincent, H.; Ibberson, R.; Audier, M.; Duboiis, J. M., *J. Phys. Condens. Mater.* **1992,** 4, 5.
10.	Petricek, V.; Gao, Y.; Lee, P.; Coppens, P., *Phys. Rev. B* **1990,** 42.
11.	Alberius-Henning, P. A.; Moustiakimov, M.; Lidin, S., Incommensurately modulated cadmium apatites. *J. Solid State Chem.* **2000,** 150, 154-158.
12.	Thompson, J. G.; Withers, R. L.; Brink, F. J., Modulated structures in oxidized cerium niobates. *J. Solid State Chem.* **1999,** 143, 122-131.
13.	Rothlisberger, F.; Seifert, F.; Czank, M., Chemical control of the commensurate-incommensurate phase transition in synthetic melilites. *Eur. J. Mineral.* **1990,** 2, 585-594.
14.	O'Keeffe, M.; Hyde, B. G., Plane nets in crystal chemistry. *A mathematical and physical science* **1980,** 295, 553-623.
15.	Li, M. R.; Kuang, X. J.; Chong, S. Y.; Xu, Z. L.; Thomas, C. I.; Niu, H. J.; Claridge, J. B.; M.J., R., Interstitial oxide ion order and conductivity in $La_{1.64}Ca_{0.36}Ga_3O_{7.32}$ melilite. *Angew. Chem. Int. Ed.* **2010,** 49, 2362 -2366.
16.	Merwin, L. H.; Sebald, A.; Seifert, F., The incommensurate-comensurate phase transition in akermanite $Ca_2MgSi_2O_7$, . *Phys. Chem. Miner.* **1989,** 16, 752-756.
17.	Hagiya, K.; Ohmasa, M., The modulated structure of synthetic Co-Akermanite, $Ca_2CoSi_2O_7$. *Acta Crystallogr. B* **1993,** 49, 172-179.
18.	Tamura, T.; Yoshiasa, A.; Iishi, K.; Takeno, S.; Maeda, H.; Emura, S.; Koto, K., Local structure of $(Ca, Sr)_2 (Mg, Co, Zn)Si_2O_7$ melilite solid-solution with modulated structure. *Phys. Chem. Miner.* **1996,** 23, 81-88.
19.	Yang, H.; Hazen, R. M.; Downs, R. T.; Finger, L. W., Structural change associated with the incommensurate-normal phase transition in akermanite, $Ca_2MgSi_2O_7$, at high pressure. *Phys. Chem. Miner.* **1997,** 24, (Springer-Verlag), 510-519.

20. Jiang, J. C.; Schosnig, M.; Schaper, A. K.; Ganster, K., Modulations in incommensurate $(Ca_{1-x}Sr_x)_2MgSi_2O_7$ single crystals. *Phys. Chem. Miner.* **1998,** 26, (Springer-Verlag), 128-134.

21. Bagautdinov, B.; Hagiya, K.; Kusaka, K.; Ohmasa, M.; Iishi, K., Two dimensional incommensurately modulated structure of $(Sr_{0.13}Ca_{0.87})_2CoSi_2O_7$ crystals. *Acta Crystallogr. B* **2000,** 56, 811-821.

22. Bindi, L.; Bonazzi, P.; Dusek, M.; Petricek, V.; Chapuis, G., Five-dimensional structure refinement of natural melilite, $(Ca_{1.89}Sr_{0.01}Na_{0.08}K_{0.02})(Mg_{0.92}Al_{0.08})(Si_{1.98}Al_{0.02})O_7$. *Acta Crystallogr. B* **2001,** 57, 739-746.

23. Tealdi , C.; Mustarelli , P.; Islam, M. S., Layered $LaSrGa_3O_7$ -based oxide-ion conductors: cooperative transport mechanisms and flexible structures. *Adv. Funct. Mater.* **2010,** XX, 1-7.

24. Thomas, C. I.; Kuang, X. J.; Deng, Z. Q.; Niu, H. J.; Claridge, J. B.; Rosseinsky, M. J., Phase stability control of interstitial oxide ion conductivity in the $La_{1+x}Sr_{1-x}Ga_3O_{7+x/2}$ melilite family. *Chem. Mater.* **2010,** 22, 2510-2516.

25. van Smaalen, S., An elementary introduction to superspace crystallography. *Z. Kristallogr.* **2004,** 219, 681-691.

26. Bruker *Topas Version 4.1*, Bruker AXS Inc.: Madison, Wisconsin, USA, 2008.

27. Cheary, R. W.; Coelho, A., A fundamental parameters approach to X-ray line-profile fitting. *J. Appl. Crystallogr.* **1992,** 25, 109-121.

28. Cheary, R. W.; Coelho, A., Axial divergence in a conventional X-ray powder diffractometer. I. Theoretical foundations. *J. Appl. Crystallogr.* **1998,** 31, 851-861.

29. Skakle, J. M. S.; Herd, R., Crystal chemistry of $(RE, A)_2 M_3 O_7$ compounds (RE= Y, lanthanide; A= Ba, Sr, Ca; M= Al, Ga). *Powder Diffraction* **1999,** 14, 195-202.

30. Petricek, V.; Dusek, M.; Palatinus, L. *Jana2006. The crystallographic computing system.*, Institute of Physics, Praha, Czech Republic, 2006.

31. Sears, V. F., *International Tables for Crystallography*. Academic Publishers: Dordrecht, Kluwer, 1993.

32. Janner, A.; Janssen, T.; de Wolff, P. M., Bravais classes for incommensurate crystal phases. *Acta Crystallogr. A* **1983,** 39, 658-666.

33. Bindi, L., When minerals become complex: an elementary introduction to superspace crystallography to describe natural-occurring incommensuartely modulated structures. *Rendiconti Lincei* **2008,** 19, (Springer-Verlag), 1-15.

34. Stokes, H. T.; Campbell, B. J.; van Smaalen, S., Generation of (3 + d)-dimensional superspace groups for describing the symmetry of modulated crystalline structures. *Acta Crystallogr. A* **2011,** 67, 45-55.

35. Shannon, R. D., *Acta Crystallogr. A* **1976,** 32.

36. Altermatt , D.; Brown, I. D., *Acta Crystallogr. B* **1985,** 41, 244-247.

37. Seifert, F.; Czank, M.; Simons, B.; Schmahl, W., A Commensurate-Incommensurate Phase Transition in Iron Bearing Akermanites. *Phys. Chem. Miner.* **1987,** 14, 26-35.

38. Jia, Z. H.; Schaper, A. K.; Treutmann, W.; Rager, H.; Massa, W., Single crystal growth and electron microscopy studies of Co/Zn-melilites with modulated structure. *J.Cryst.Growth* **2004,** 273, 303-310.

39.   Seifert, F.; Rothlisberger, F., Macroscopic and structural changes at the incommensurate-normal phase transition in melilites. *Mineralogy and Petrology* **1993,** 48, 179-192.

40.   Wong, C. L.; Ferraris, C.; White, T. J., Microstructural features and domain formation in $(Ba,Sr)_2TiSi_2O_8$ fresnoites. *J. Solid State Chem.* **2011,** 184, 1768-1776.

41.   Santamaria-Perez, D.; Vegas, A., The zintl-klemm concept applied to cations in oxides. I. The structures of ternary aluminates. *Acta Crystallogr. B* **2003,** 59, 305-323.

42.   Moore, P. B.; Louisnathan, J., Fresnoite: unusual titanium coordination. *Science* **1967,** 156, 1361-1362.

43.   Zid, M. F.; Jouini, T., $K_2MoO_2As_2O_7$. *Acta Crystallogr.C* **1996,** 52, 1334-1336.

44.   Chakoumakos, B. C.; Cutselcean, R.; Kamiyama, T.; Oikawa, K.; Sales, B. C.; Lumsden, M. D., Structural modulation in $K_2V_3O_8$. *J. Solid State Chem.* **2007,** 180, 812-817.

45.   Byström, A. M.; Evans, H. T. J., The crystal structure of $K_3V_5O_{14}$. *Acta Chem.Scand.* **1959,** 13, 377-378.

46.   Johnberg, L., Crystal structures of $Na_2Nb_4O_{11}$ and $CaTa_4O_{11}$. *J. Solid State Chem.* **1970,** 1, 454-462.

47.   Shannon, J.; Katz, L., The structures of the reduced and oxidized forms of barium silicon tantalum oxide, $Ba_3Si_4Ta_6O_{23}$ and $Ba_3Si_4Ta_6O_{26}$. *J. Solid State Chem.* **1970,** 1, 399-408.

48.   Stephenson, N. C.; Roth, R. S., Structural systematics in the binary system Ta_2O_5-WO_3. V. the structure of the low-temperature form of tantalum oxide L-Ta_2O_5. *Acta Crystallogr. B* **1971,** 27, 1037-1044.

49.   Marnider, B., Some complex structures built up of modules obtained from the R-Nb_2O_5 structure through chemical twinning. *Acta Chem. Scand.* **1990,** 44, 123-134.

50.   Liu, F.; Garofalini, S. H.; King-Smith, R. D.; Vanderbilt, D., Structural and electronic properties of sodium metasilicate. *Chem. Phys. Lett.* **1993,** 215, 401-404.

51.   Martin-Sedeno, M. C. e. a., Structural and electrical investigation of oxide ion and proton conducting titanium cuspidines. *Chem. Mater.* **2005,** 17, 5989-5998.

52.   Gesing, T. M.; Uecker, R.; Buhl, J. C., Crystal structure of distrontium lanthanum gallium pentaoxide Sr_2LaGaO_5. *Eitschrift fuer Kristallographie - New Crystal Structures* **2002**.

53.   Armbruster, T., Layer topology, stacking variation and site distortion in melilite-related compounds in the system CaO-ZnO-GeO_2-SiO_2. *Am. Mineral.* **1990,** 75, 847-858.

54.   Fleet, M. E.; Henderson, G. S., Epsilon sodium silicate : a high-pressure layer structure $(Na_2Si_2O_5)$. *J. Solid State Chem.* **1995,** 119, 400-404.

55.   Goreaud, M.; Choisnet, J.; Raveau, B.; Deschanvres, A., Sur les silicogermanates $Ba (Si_{2-x} Ge_x) O_5$ isotypes de la sanbornite. *Revue de Chimie Minerale* **1974,** 11, 207-216.

56.   Bakakin, V. V.; Belov, N. V.; Borisov, S. V.; Solovyeva, L. P., Crystal structure of nordite and its relationship to melilite and datolite-gadolinite. *Am. Mineral.* **1970,** 55, 1167.

57.   Belokoneva, E. L.; Stefanovich, S. Y.; Pisarevskii, Y. V.; Mosunov, A. V., Refined structures of $La_3Ga_5SiO_{14}$ and $Pb_3Ga_2Ge_4O_{14}$ and the crystal-chemical regularities in the structure and properties of compounds of the langasite family. *Russ. J. Inorg. Chem.* **2000,** 45, 1642-1651.

58.   Bindi, L.; Dusek, M.; Petricek, V.; Bonazzi, P., Superspace-symmetry determination and multi-dimensional refinement of the incommensurately modulated structure of natural fresnoite. *Acta Crystallogr. B* **2006,** 62, 1031-1037.

59.   Pérez, O.; Malo, S.; Hervieu, M., The modulated structure of the calcium aluminate $Ca_6(AlO_2)_{12}$-Bi_2O_3. *Acta Crystallogr. B* **2010,** 66, 585-593.

60.   Krüger, H.; Kahlenberg, V.; Friese, K., $Na_2Si_3O_7$: an incommensurate structure with crenel-type modulation functions, refined from a twinned crystal. *Acta Crystallogr. B* **2006,** 62, 547-555.

61.   Krüger, H.; Kahlenberg, V., Incommensurately modulated ordering of tetrahedral chains in $Ca_2Fe_2O_5$ at elevated temperatures. *Acta Crystallogr. B* **2005,** 61, 656-662.

62.   Hayward, M. A.; Rosseinsky, M. J., Cool Conditions for Mobile Ions. *Nature* **2007,** 450, 960-961.

63.   Inoue, S.; Kawai, M.; Ichikawa, N.; Kageyama, H.; Paulus, W.; Shimakawa, Y., Anisotropic oxygen diffusion at low temperature in perovskite-structure iron oxides. *Nature Chem.* **2007,** 2, 213-217.

Table of Content Graphic

The Five-Dimensional Incommensurate Structure of the Melilite

Electrolyte $[CaNd]_2[Ga]_2[Ga_2O_7]_2$

Fengxia Wei[a], Tom Baikie[a], Tao An[a], Martin Schreyer[b], Christian Kloc[a] and Tim. J. White[a,c]